Advanced Functional Materials

ADVANCED FUNCTIONAL MATERIALS
www.afm-journal.de

RESEARCH ARTICLE

Unusual Strain Relaxation and Dirac Semimetallic Behavior in Epitaxial Antiperovskite Nitrides

Ting Cui[1,2] | Zihan Xu[3] | Qinghua Zhang[1] | Ying Zhou[4] | Xiaodong Zhang[3] | Qianying Wang[1,2] | Dongke Rong[1,2] | Songhee Choi[1] | Axin Xie[1,2] | Hongyun Ji[1,2] | Can Wang[1,2] | Chen Ge[1,2] | Hongjian Feng[3] | Shanmin Wang[5] | Shuai Dong[4] | Kuijuan Jin[1,2] | Liang Si[3,6] | Er-Jia Guo[1,2]

[1]Beijing National Laboratory for Condensed Matter Physics and Institute of Physics, Chinese Academy of Sciences, Beijing, China | [2]Department of Physics & Center of Materials Science and Optoelectronics Engineering, University of Chinese Academy of Sciences, Beijing, China | [3]School of Physics, Northwest University, Xi'an, China | [4]School of Physics, Key Laboratory of Quantum Materials and Devices of Ministry of Education, Southeast University, Nanjing, China | [5]Department of Physics, Southern University of Science and Technology, Shenzhen, China | [6]Shanxi Key Laboratory for Theoretical Physics Frontiers, Xi'an, China

Correspondence: Shuai Dong (sdong@seu.edu.cn) | Kuijuan Jin (kjjin@iphy.ac.cn) | Liang Si (siliang@nwu.edu.cn) | Er-Jia Guo (ejguo@iphy.ac.cn)

Received: 9 December 2025 | **Revised:** 2 March 2026 | **Accepted:** 11 March 2026

Keywords: antiperovskite nitrides | dirac semimetal | interfacial strain accommodation | Ni_3InN

ABSTRACT

Antiperovskite nitrides (X_3AN) serve as both structural and conceptual counterparts to the extensively studied perovskite oxides. However, their epitaxial stabilization and the associated emergent electronic properties remain largely unexplored. Here, we report the successful growth of Ni_3InN thin films on perovskite substrates with lattice constants ranging from 3.78 to 3.98 Å. First-principles phonon calculations confirm the dynamical stability of cubic phase Ni_3InN, providing the basis for epitaxial synthesis. High-resolution scanning transmission electron microscopy reveals (001)-oriented coherent interfaces when Ni_3InN is grown on $LaAlO_3$ and $SrTiO_3$, while the growth on $DyScO_3$ results in an unexpected (011)-oriented interface, consistent with surface-energy calculations. Transport measurements highlight a strain-controlled within a Fermi-liquid behavior, which correlates with variations in Ni-3*d* bandwidth, Ni-3*d*/N-2*p* hybridization. Band structure calculations reveal a unique dual contribution near the Fermi level: a Dirac-like dispersion that supports high mobility and a Ni-3*d*-derived manifold that governs strange-metal transport, exhibiting a reduced slope compared to oxide perovskites. Notably, the formal Ni valence (∼+2/3) places Ni_3InN within an overdoped correlated-metal regime, distinguishing it from most oxide perovskites. This positions antiperovskite nitrides as a promising platform for investigating overdoped Fermi liquids and strange-metal behavior.

1 | Introduction

The search for emergent quantum states in correlated electron systems continues to be at the forefront of condensed matter physics. Many of these states—such as unconventional superconductivity [1, 2], colossal magnetoresistance [3, 4], and Fermi-liquid transport [5, 6]—emerge from the complex coupling between various physical degrees of freedom, including charge, spin, orbital, and lattice. Perovskite oxides, with the general formula ABO_3 (Figure 1a), have long served as a canonical platform for exploring these phenomena. For example, interface engineering in $ABO_3/A'B'O_3$ heterostructures has facilitated the discovery of 2D electron gases and their associated superconductivity [7, 8]. The synthesis of thin films along unconventional crystallographic

Ting Cui, Zihan Xu, and Qinghua Zhang contributed equally to this work

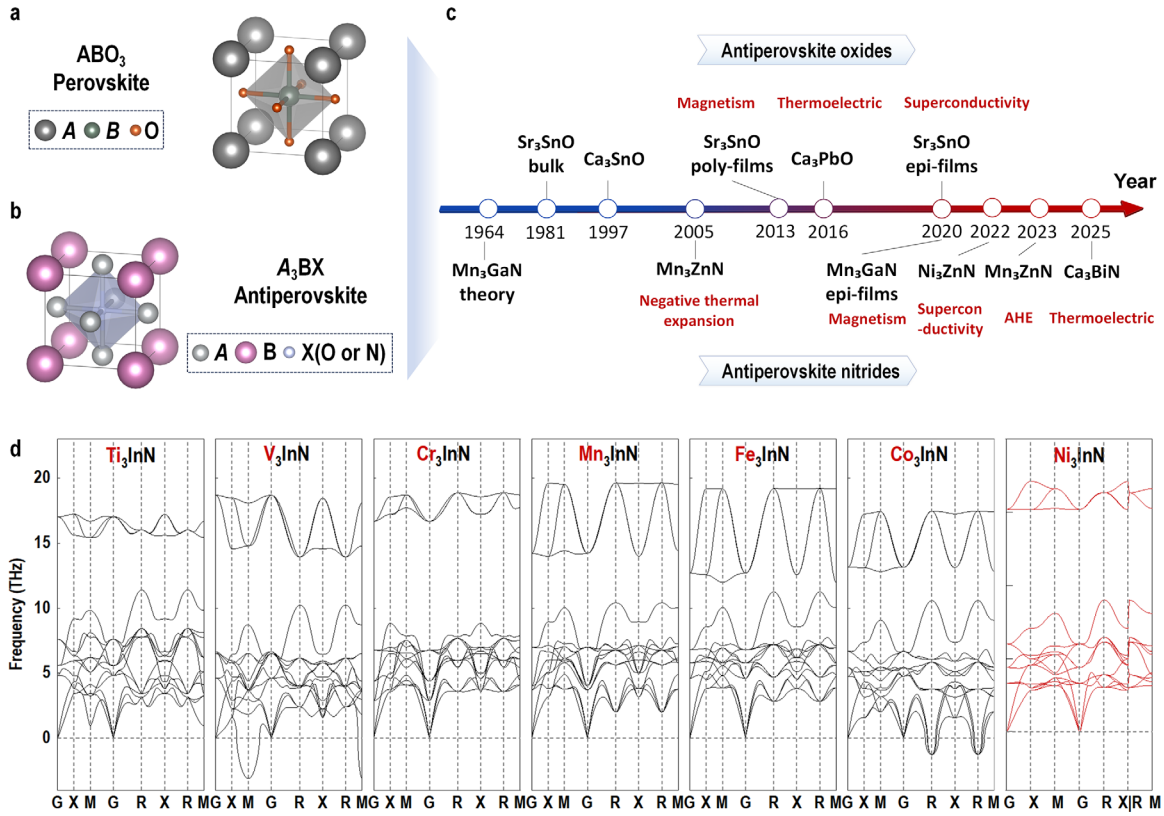

FIGURE 1 | Evolution of antiperovskite-type materials. Schematic illustrations of the crystal structures of (a) perovskite (ABX_3, where X = O or N) and (b) antiperovskite (A_3BX, where X = O or N) oxides/nitrides. (c) Timeline of the discovery of key physical properties in antiperovskite oxides and nitrides. (d) DFT phonon spectra for A_3InN antiperovskite nitrides, including Ti_3InN, V_3InN, Cr_3InN, Mn_3InN, Fe_3InN, Co_3InN and Ni_3InN, where V_3InN and Co_3InN are dynamically unstable.

orientations (e.g., [110] or [111]) has led to the revelation of novel orbital and topological states [9, 10]. Additionally, (original and reduced) Ruddlesden–Popper (RP) phases, such as $La_3Ni_2O_7$, and $La_4Ni_3O_{10}$, have recently uncovered unconventional high-temperature superconductivity [11–14]. More strikingly, topotactic reduction from ABO_3 to ABO_2 phases has stabilized new electronic ground states, as exemplified by superconductivity in the hole-doped infinite-layer nickelates $(Nd,Sr)NiO_2$ [15, 16]. These advances highlight the perovskite framework as a versatile platform for emergent phases, enabled by structural flexibility, heterostructure engineering, and symmetry breaking.

Inspired by these advances, a key direction is to explore material families that share structural motifs with perovskites but have been comparatively less studied. Unlike their perovskite counterparts, antiperovskites with the general formula of A_3BX (X = O or N) feature inverted positions of cations and anions (Figure 1b). However, this inversion is difficult to achieve in oxides due to the small ionic size and high electronegativity of the O^{2-} anion. These limitations cause structural and electrostatic instabilities and make it difficult to maintain charge balance with suitable cations [17]. Figure 1c presents the development timeline of both antiperovskite oxides and nitrides. Notably, only a limited number of antiperovskite oxides, including Sr_3SnO, Ca_3SnO, and Sr_3PbO, have been successfully stabilized and reported to date [18–20]. The magnetism, thermoelectric, and superconductivity have been investigated in these antiperovskite oxides over decades. Compared to oxides, nitrides with antiperovskite structure are more readily formed [21–24]. It preserves the favorable electrostatic and geometric coordination with low-valence metal cations. The partial covalency of metal–nitrogen bonds and the availability of suitable synthetic routes make nitrides more structurally and chemically compatible with the antiperovskite framework. Despite their simple cubic symmetry, anti-perovskite nitrides host a wide variety of intriguing states [25–28]. Examples include negative thermal expansion in Mn_3ZnN, electron-phonon mediated superconductivity in Ni_3ZnN [21], and exotic topological band structures in Ca_3BiN and related compounds [29]. Mn_3GaN, first predicted in 1964, then has been studied foritsr non-collinear antiferromagnetism and large anomalous Hall effects, which are highly relevant for spintronic applications [28, 30–32]. From a practical application point of view, the negative thermal expansion behavior in antiperovskite nitrides can be useful for thermal management and as components in a composition to compensate for expansion. The excellent mechanical and thermodynamic stability makes thembeneficialt for device integration [33]. Thus, these advantages make them a compelling complementary system to conventional perovskite oxides. Yet, compared with the vast body of work on perovskite oxides, the epitaxial growth, interface engineering, and correlated-electron properties of antiperovskite nitrides remain largely unexplored.

In this work, we use Ni_3InN as a model system to demonstrate epitaxial thin-film growth and strain-mediated physical

properties in a dynamically stable antiperovskite nitride. We revealed distinct strain relaxation behavior that contrasts sharply with conventional perovskite oxides. This behavior arises from a combination of its high structural rigidity and reduced surface formation energy of the (011) facet under tensile strain. We found that the strain triggers the transition in the low-temperature transport behavior, which correlates with changes in Ni-3*d* bandwidth and Ni-3*d*/N-2*p* hybridization. Importantly, the formal Ni valence in Ni_3InN is approximately + 2/3. This places the system in a heavily over-doped regime that is rarely accessible in perovskite oxides, where transition-metal valences are typically closer to integer values. This renders antiperovskite Ni_3InN a natural platform for exploring over-doped correlated metals and testing theoretical models of Fermi-liquid stability.

2 | Results and Discussions

2.1 | Synthesis and Characterization of Antiperovskite Nitride Ni_3InN Thin-Films

To confirm the stability and well-defined lattice structure of indium-based antiperovskite nitrides, X_3InN ($X = 3d$ elements), we first calculated the phonon spectra of all indium-based antiperovskite nitrides (Figure 1d) containing 3*d* elements (for computational details, see Method). The results show that the spectra of Ti_3InN, Cr_3InN, Mn_3InN, Fe_3InN, and Ni_3InN show a complete absence of imaginary modes throughout the Brillouin zone, confirming their dynamical stability, whereas V_3InN and Co_3InN exhibit dynamical instabilities with imaginary frequencies in their phonon spectra. For Ni_3InN, the phonon density of states further reveals that the lighter N atoms dominate the high-frequency modes (around 16 THz), whereas the heavier Ni and In atoms, coupled with N, govern the low-frequency region below 8 THz (Figure S1). Such a distribution is characteristic of intermetallic systems, in which N atoms are embedded within a covalently bonded In–Ni sublattice. This finding not only validates the dynamical stability of Ni_3InN but also underscores its strong potential for experimental synthesis and functional applications.

To synthesis the high-quality Ni_3InN, we first fabricated a stoichiometric Ni_3InN ceramic target using a high-pressure and high-temperature synthesis approach. The XRD results identify its correct crystallinity and pure phase (Figure S2). Subsequently, Ni_3InN thin films were grown on $LaAlO_3$, $SrTiO_3$, and $DyScO_3$ substrates via pulsed laser deposition (PLD) (see Method). The calculated misfit strains $\varepsilon = (a_{sub} - a_{film})/a_{film} \times 100\%$, are $\varepsilon = -1.30\%$, 1.69%, 2.81% for $LaAlO_3$, $SrTiO_3$, and $DyScO_3$ substrates, respectively. Interestingly, X-ray diffraction θ–2θ scans (Figure 2a) reveal that Ni_3InN films grown on $LaAlO_3$ and $SrTiO_3$ substrates exhibit a (001)-oriented phase, whereas the Ni_3InN film on $DyScO_3$ substrate shows an unconventional (011) orientation. X-ray absorption spectroscopy (XAS) was performed to analyze the elemental composition of the Ni_3InN thin films (Figure S3). Spectra collected at the N *K*- and Ni *L*-edges indicated a significant presence of nitrogen in the films, and a minor fraction of Ni^{2+} suggested slight surface oxidation of the Ni_3InN layers. To further investigate the atomic-scale structure of representative films, we performed high-resolution scanning transmission electron microscopy (STEM) imaging on these two Ni_3InN thin films. Integrated differential phase contrast (iDPC) imaging, shown in Figure S4, clearly reveals N atoms are located at the body-centered positions. Figure 2b presents a representative high-angle annular dark-field (HAADF) image of a (001)-oriented Ni_3InN film grown on $SrTiO_3$, with the inset showing the corresponding unit cell. Figure 2c displays a similar HAADF-STEM image of a (011)-oriented Ni_3InN film on $DyScO_3$, with the inset providing a magnified view of the unit cell. Both images unambiguously confirm the excellent crystallinity of Ni_3InN films grown on different substrates, as evidenced by the well-defined atomic arrangements, minimal disorder, and sharp diffraction contrast in the HAADF images. These findings stand in stark contrast to conventional perovskite oxide films, which are epitaxially grown on substrates that induce different strain states (Figure S5). For perovskite oxides, the out-of-plane lattice constants typically vary systematically with in-plane strain, resulting in elastic structural deformations. However, the growth orientation of Ni_3InN films is strongly influenced by the strain state of the underlying substrates. Figure 2d illustrates the (001)-oriented growth of Ni_3InN under compressive strain ($\varepsilon < 0$), where the film remains constrained by the substrate. In contrast, when grown on substrates with significant tensile strain, the film undergoes strain relaxation, leading to a preferential [011] orientation (Figure 2e).

In the thin-film growth, the substrates' induced strain strongly influences which crystallographic orientation is more energetically favorable. To analyze this mechanism, the surface formation energy (E_{surf}) was calculated for two possible orientations, [001] and [011], of Ni_3InN films. The surface formation energy essentially measures the energetic cost of creating and maintaining a given crystallographic surface under specific strain conditions. The orientation with the lower surface formation energy is thermodynamically more stable and thus more likely to occur experimentally. As shown in Figure 2f, under compressive strain and moderate tensile strain, the [001] orientation has lower E_{surf}. The films naturally stabilize in this orientation when grown on substrates imposing these strain states (e.g., $LaAlO_3$ and $SrTiO_3$). Under significant tensile strain, however, the [011] orientation becomes energetically more favorable than the (001). This indicates that the crystal structure of Ni_3InN relaxes more effectively in the [011] orientation when subjected to strong tensile strain (e.g., $DyScO_3$). Importantly, this theoretical explanation matches our experimental observations. Thereby, these calculations provide strong evidence that the unconventional orientation transition is driven by strain-mediated energetics, establishing a clear mechanism for controlling crystalline orientation in antiperovskite nitride films.

On the other hand, we also calculated the mechanical properties of bulk Ni_3InN and extended the comparative analysis to other X_3InN compounds. Figure 2g presents the calculated elastic constants C_{11}, C_{12}, and C_{44} for bulk X_3InN, obtained via using density-functional theory (DFT). All X_3InN compounds exhibit enhanced C_{11}, reflecting strong resistance to uniaxial compression, while their C_{44} values are significantly reduced, indicating diminished shear rigidity. From a structural perspective, this behavior arises from the robust covalent interactions in the In—N and *X*—N bonding networks, which dominate the longitudinal response. In contrast, shear deformations preferentially activate

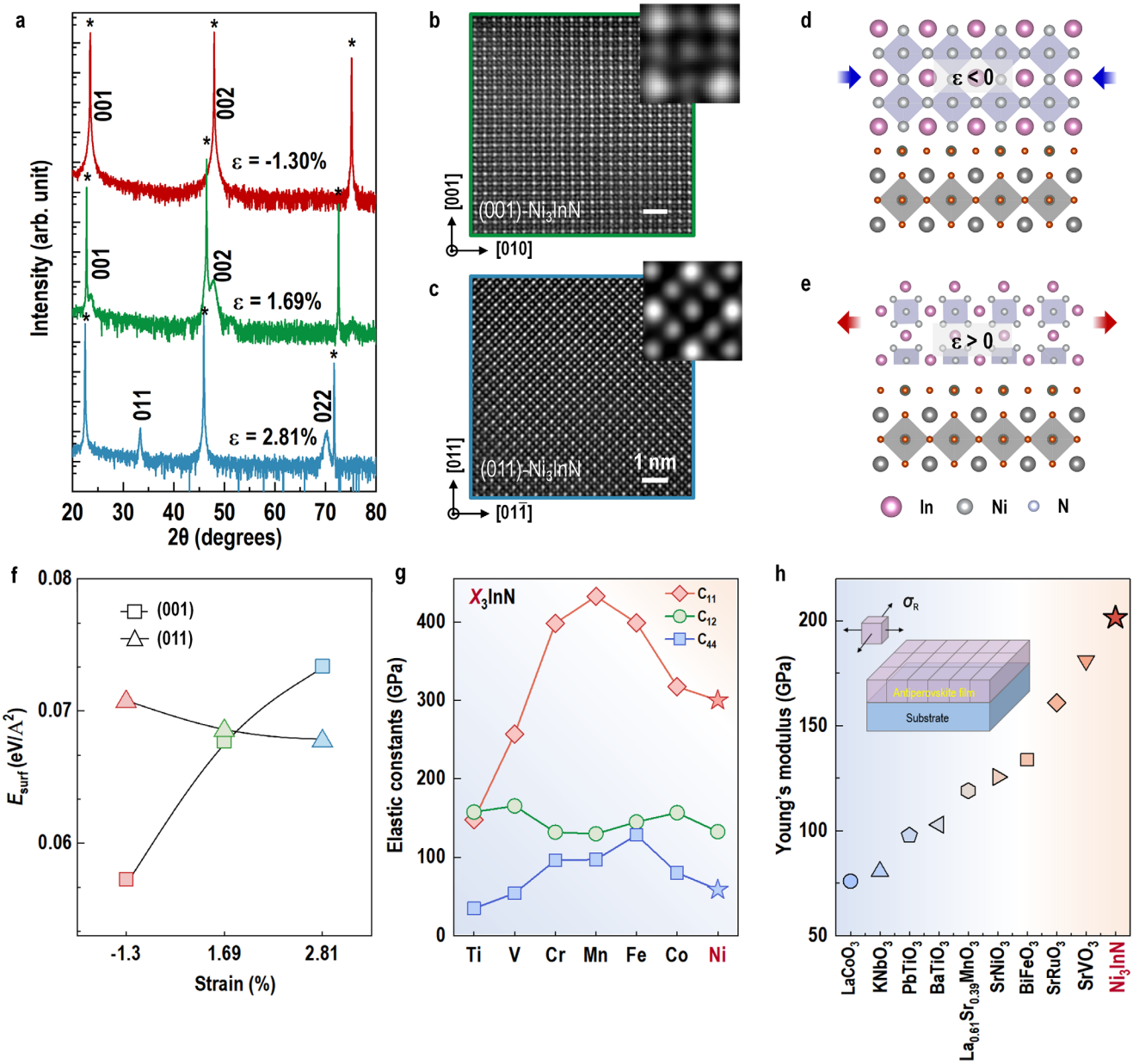

FIGURE 2 | Structural characterization of Ni_3InN thin films. (a) X-ray diffraction θ–2θ scans of Ni_3InN films grown on $LaAlO_3$ ($\varepsilon = -1.30\%$), $SrTiO_3$ ($\varepsilon = 1.69\%$), and $DyScO_3$ ($\varepsilon = 2.81\%$) substrates (indicated with "*"). (b) High-resolution HAADF-STEM image from a (001)-oriented Ni_3InN film grown on $SrTiO_3$. Inside shows a representative unit cell. (c) HAADF-STEM image of (011)-oriented Ni_3InN film on $DyScO_3$, inset showing a magnified unit cell. (d,e) Schematic illustrations of [001]-oriented Ni_3InN grown under compressive-strain ($\varepsilon < 0$) and [011]-oriented Ni_3InN grown under tensile strain ($\varepsilon > 0$). (f) Formation energy E_{surf} of (001)- and (011)-oriented Ni_3InN under different strain states. (g) Calculated elastic constants C_{11}, C_{12}, and C_{44} of X_3InN as a function of X-site composition (X = Ti, V, Cr, Mn, Fe, Co, Ni). Ni_3InN exhibits higher C_{11} and lower C_{44}, pointing to enhanced longitudinal stiffness but reduced shear rigidity. (h) Comparison of Young's modulus of Ni_3InN with the previously reported conventional perovskite oxides, indicating that Ni_3InN possesses enhanced mechanical rigidity comparable to the extensively studied perovskite oxides. The inset in (h) illustrates a schematic diagram of the equibiaxial tensile strain applied to the film by the substrate.

lower-energy octahedral tilting or rotational modes, a hallmark of perovskite-type frameworks [34, 35]. To further quantify these characteristics, the Young's modulus of Ni_3InN was directly compared with those of conventional perovskite oxides. (Figure 2h and Table 1) [36–43]. The inset illustrates the strain state of an antiperovskite film grown on a single-crystalline substrate, where σ^R denotes equibiaxial tensile stress. Notably, Ni_3InN exhibits a remarkably high Young's modulus (~201.5 GPa), underscoring its capability to not only match but potentially surpass conventional perovskite oxides in mechanical properties. In addition, we find that the substantial C_{11} value suggests high speed of sound and superior thermal conductivity due to strong bond stiffness, confirming the large stiffness of Ni_3InN. Furthermore, Ni_3InN exhibits a Poisson's ratio of 0.33, closely comparable to that of stainless steel (0.30–0.31) and characteristic of ionic–covalent solids and metallic alloys [44–49]. This correspondence indicates that Ni_3InN can maintain mechanical stability under both in-plane and hydrostatic stress conditions.

TABLE 1 | Summary of Young modulus for conventional perovskite oxides and antiperovskite nitride Ni_3InN presented in this work.

Materials	Young modulus/GPa	Refs.
$LaCoO_3$	76	[37]
$KNbO_3$	80.64	[41]
$PbTiO_3$	97.75	[41]
$BaTiO_3$	102.9	[41, 43]
$La_{0.61}Sr_{0.39}MnO_3$	120	[38, 39]
$BiFeO_3$	133.73	[42]
$SrRuO_3$	161	[40]
$SrVO_3$	181.1	[36]
Ni_3InN	201.5	/

2.2 | Microstructure and Epitaxial Relationship of Ni_3InN/Perovskite Oxides Heterostructures

The unique strain relaxation behavior suggests that the interface structure of Ni_3InN may be established early in the thin-film growth process. To further probe the atomic-scale interface structure and epitaxial relationships of Ni_3InN films on various substrates, we employed a combination of high-resolution STEM and electron energy-loss spectroscopy (EELS). Low-magnification HAADF-STEM images for Ni_3InN films were provided in Figure S6. In addition, the interfacial atomic configurations and corresponding intensity line profiles along the growth direction for three Ni_3InN films were compared in Figure S7. The compressively strained Ni_3InN films exhibit coherent epitaxy along the [001] direction with a characteristic $a/2$ in-plane lattice offset and an ultrathin transition layer with a thickness of approximately 0.24 nm (Figure 3a). The atomic resolution EELS analysis demonstrates an InNi-LaO interfacial configuration (Figure 3d) to compensate for the interfacial charge imbalance. The [001] orientation persists under moderate tensile strain ($\varepsilon = 1.69\%$) despite an increased interfacial gap distance of approximately 0.76 nm (Figure 3b). The interface termination changes to a distinct InNi-TiO_2 (Figure 3e). We further observed that the unit cells of Ni_3InN undergo periodic lateral realignment with a characteristic period of ~11.7 nm, corresponding to 30 unit cells of $SrTiO_3$ (Figure S8). This periodicity can be quantitatively accounted for by the lattice constant mismatch between Ni_3InN and the substrate. Further increasing the tensile strain induces a complete orientation transition to [011], accompanied by interfacial gap distance expansion to 1.05 nm (Figure 3c). Figure 3f summarizes a strong correlation between interfacial gap distance and misfit strain, with gap expansion from 0.24 to 1.05 nm as strain increases from -1.3% (compressive) to +2.81% (tensile). The c/a ratios derived from HADDF-STEM images consistently approach unity ($c/a \approx 1$), unambiguously demonstrating the exceptional structural stability of Ni_3InN under various strain states. The strain distributions within Ni_3InN films grown on three different substrates were analyzed along both the in-plane and out-of-plane directions (Figures S9–S11). The results reveal that strain relaxation occurs locally at the heterointerface on the nanometer scale.

The narrow strain accommodation window and abrupt structural transitions contrast sharply with the gradual interfacial evolution observed in perovskite oxides. In perovskite oxides, lattice mismatch with the substrate is typically accommodated through continuous elastic deformation of the lattice, enabled by the flexibility of corner-sharing octahedral frameworks that can tilt and rotate over a wide strain range. In some cases, the substrate-induced epitaxial strain can persist over a hundred nanometers [50, 51]. In contrast, the Ni_3InN films do not rely on gradual lattice distortion to relieve strain. Instead, once a critical strain threshold is exceeded, the system undergoes abrupt relaxation processes, such as an orientation transition from (001) to (011), reflecting the more rigid bonding environment of the intermetallic In–Ni sublattice in which N atoms are embedded. We attribute this anomalous strain response in Ni_3InN likely stems from its exceptional mechanical stiffness, revealing a new paradigm for strain engineering in hard, covalent antiperovskite systems.

2.3 | Exceptional Electronic Stability of Strained Ni_3InN Films

To explore the impact of strain on the transport and optical properties of Ni_3InN, we employed DFT to compute the electronic band structure, density of states (DOS), Fermi surface, and edge state (Figure S12a–d). As shown in Figure 4a and Figure S12a–c, the band structure reveals that empty In-p and fully occupied N-p orbitals correspond to an In^{1+}/N^{3-} configuration, leading to a nominal Ni valence of +⅔. This unusual low valence of Ni, stabilized by the antiperovskite lattice, may underlie moderate correlations, emergent magnetic or electronic behaviors distinct from conventional $ANiO_X$ and nickelate materials. Without spin–orbit coupling (SOC), Ni_3InN exhibits a closed bandgap, with the bands crossing the Fermi level along R–X and near the M point, indicating metallic behavior. Notably, band inversion and two Dirac-like nodes appear near the M point and Fermi level (Figure 4a,b). Including SOC opens a hybrid bandgap in the inverted region via N-p and Ni-d orbital hybridization. Tight-binding calculations confirm the emergence of boundary states (Figure S12d), suggesting Ni_3InN supports a quantum-spin-Hall-like (QSH) phase that is typically linked to high conductivity and mobility, as seen in topological systems like graphene and semimetals [52, 53]. The calculated 3D band structure (Figure 4b) and Fermi surface (Figure S12c) shows an anisotropic character, with distinct electron pockets and critical points along different crystallographic directions, highlighting the interplay between symmetry and transport anisotropy.

Temperature-dependent resistivity (ρ) measurements on three strained Ni_3InN thin films (Figure 4c) reveal nearly constant ρ across the full temperature range, with only a slight upturn below 20 K, indicating Fermi-liquid transport character. The high-temperature resistivity is exceptionally stable, with a slope of $\sim 2.02 \times 10^{-8}$ Ω·cm/K, outperforming most reported antiperovskite nitrides [17, 54–56]. Our transport calculations (Figure S13) align well with experimental trends and low-temperature behavior. θ–2θ scans (Figure S14) confirm structural stability from 10 to 300 K, showing only minor thermal expansion along the c-axis. Hall measurements (Figure S15) indicate that carrier density

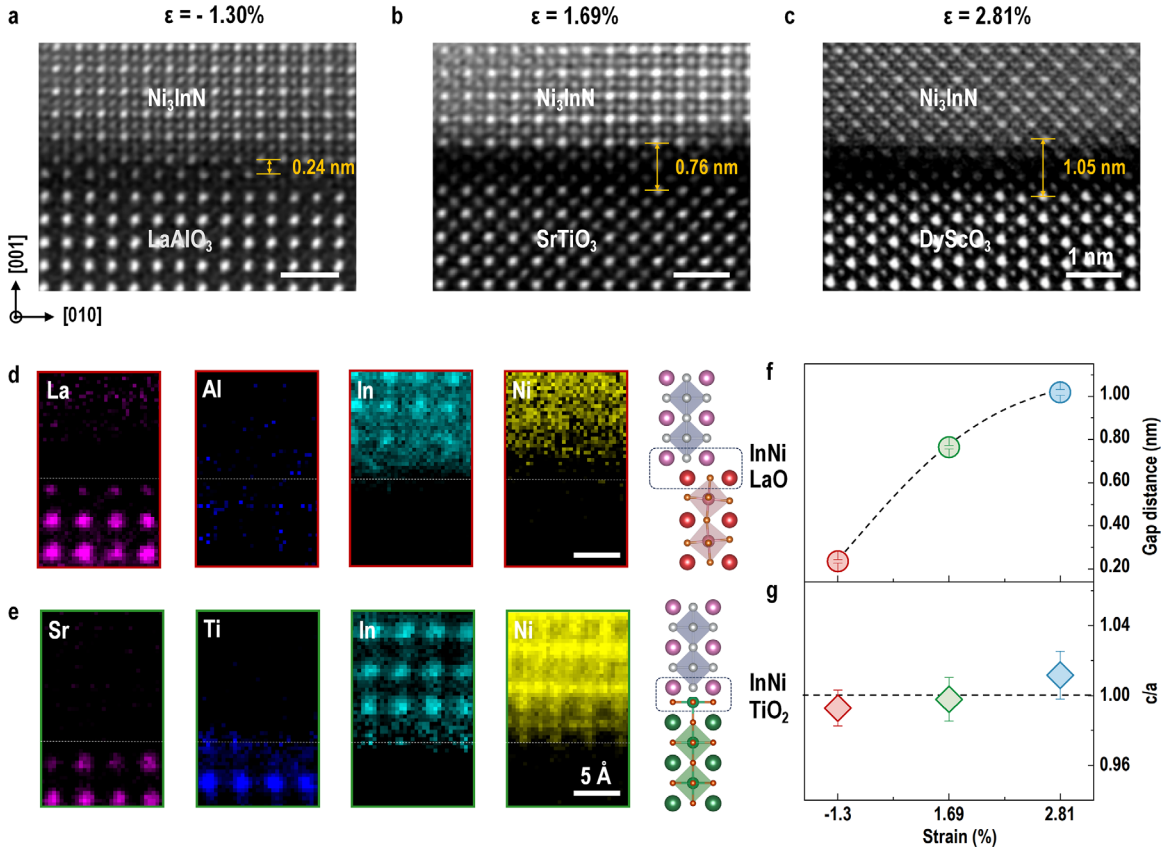

FIGURE 3 | Atomic-scale characterization of Ni_3InN interfacial structures on three distinct substrates. (a–c) HAADF-STEM images of the Ni_3InN thin films grown on $LaAlO_3$, $SrTiO_3$, and $DyScO_3$ substrates taken along the [100] zone axis. The interfacial regions with variable gap distances are annotated in yellow. (d) Compositional EELS mapping of $Ni_3InN/LaAlO_3$ taken simultaneously at La *M*-, Al *K*-, In *M*-, and Ni *L*-edges, respectively. Representation of the $Ni_3InN/LaAlO_3$ heterointerface as a stacking of atomic unit cell planes, showing a half-unit-cell lateral lattice misalignment between adjacent atomic planes. (e) Atomic-scale EELS mapping of $Ni_3InN/SrTiO_3$ taken simultaneously at Sr *L*-, Ti *L*-, In *M*-, and Ni *L*-edges, respectively. Ni_3InN is epitaxially grown on $SrTiO_3$ via cube-on-cube orientation. (f) Gap distances between Ni_3InN thin films and substrates as functions of strain. (g) Strain-dependent *c*/*a* ratio of Ni_3InN thin films.

(n) in films on $LaAlO_3$ remains stable at $(5.69–6.49) \times 10^{22}$ cm^{-3}, with mobility (μ) nearly temperature-independent (Figure S16). Under compressive strain, n peaks while μ is minimized; tensile strain reduces n and enhances μ. On $SrTiO_3$ and $DyScO_3$ substrates, n decreases and μ increases with temperature due to a stronger correlation in Ni-3*d*. These findings suggest that the combination of structural robustness and Dirac metallicity drives the remarkable resistivity stability—an intrinsic property of Ni_3InN thin films. High-temperature ρ–T curves show linear behavior, indicating conduction dominated by Ni-3*d* bands and "*strange metal*" characteristics. Under increasing tensile strain, the ρ–T slopes increase slightly but remain far below those in oxide perovskites (Figure 4c). The low Ni valence (~+⅔) places Ni_3InN in an overdoped correlated-metal regime. At low temperatures (20–65 K), $\rho(T)$ fits well to $\rho(T) = \rho_0 + AT^2$, with $\rho_0 \approx 1.55 \times 10^{-4}$ Ω·cm and $A \approx 2.27 \times 10^{-10}$ Ω·cm/K^2, consistent with Fermi liquid behavior. Under tensile strain, reduced Ni-*d* bandwidth enhances correlations, yielding more pronounced Fermi liquid signatures, particularly on DSO substrates. Optical conductivity measurements confirm multiple interband excitations. In addition to a dominant Drude peak (t_{2g}–t_{2g} transitions), four peaks arise from e_g–t_{2g}, t_{2g}–In5*p*, e_g–In5*p*, and N2*p*–t_{2g} transitions, consistent with band structure and DOS calculations.

Electronic structure analysis reveals two main Fermi-level contributions: temperature-independent QSH-like edge states and bulk states near the R–X point that are temperature-dependent. At high temperatures, all films exhibit "*strange metal*" behavior with smaller ρ–T slopes than in oxide perovskites, suggesting a distinct origin rooted in anti-perovskite topology. The coexistence of these two channels explains Ni_3InN's unique transport: robust, high-mobility conduction from boundary states and tunable, strain-sensitive behavior from bulk bands.

3 | Summary and Outlooks

In summary, the stabilization of a rare low-valence state of Ni, pronounced longitudinal rigidity, and a Young's modulus comparable to many functional substrate materials make Ni_3InN as a highly promising electronic and mechanically robust antiperovskite nitride. We have successfully fabricated high-quality single-crystalline Ni_3InN thin films on various substrates and demonstrated the unique strain relaxation mechanisms governed by the material's exceptional stiffness and intrinsic orientation preferences, which sharply differ from conventional perovskite oxides. Atomic-resolution analysis not only confirms

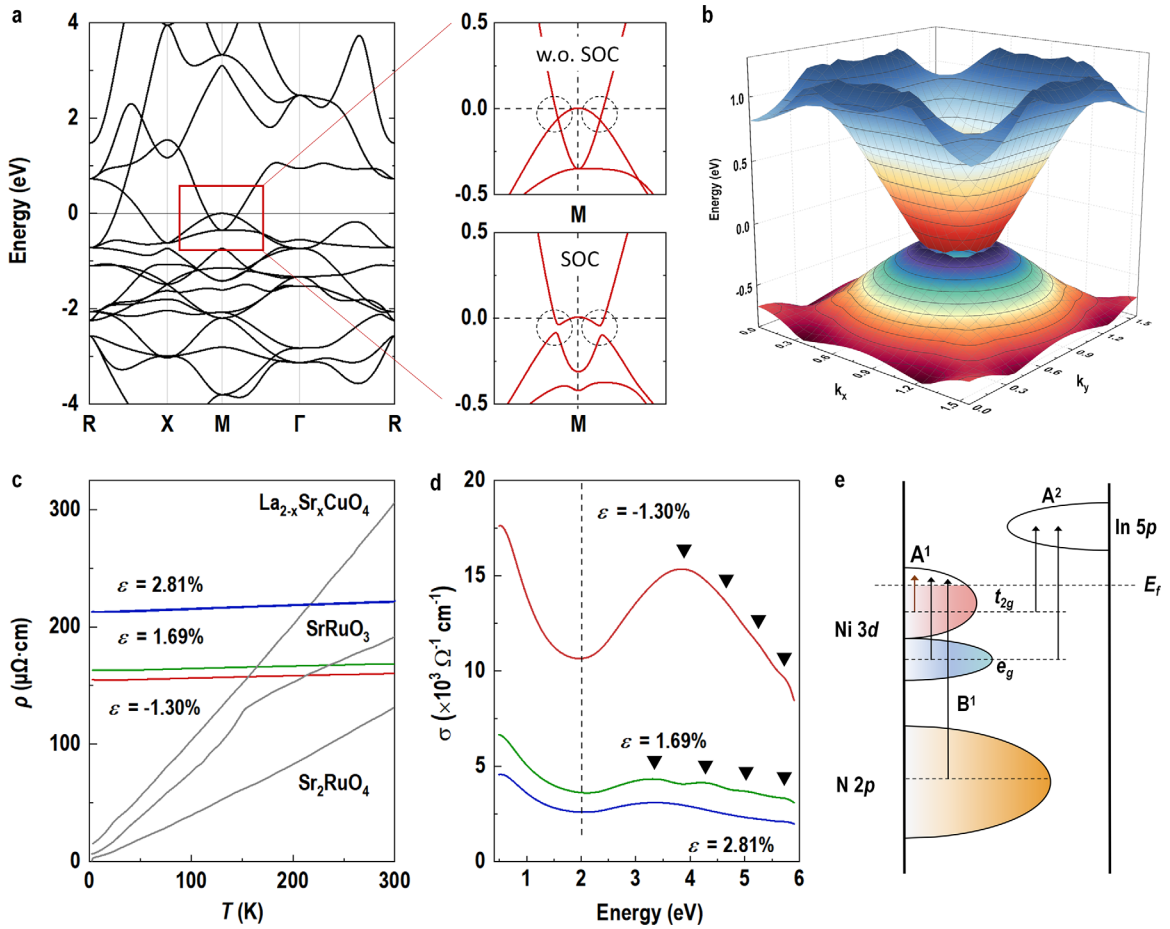

FIGURE 4 | Band structure calculations and electronic properties of Ni_3InN. (a) DFT band structure of Ni_3InN highlighting empty In-*p* states and fully filled N-*p* bands, consistent with an In^{1+}/N^{3-} charge state and an average Ni valence of $Ni^{+2/3}$. The right side presents the band structures around the M point without (w.o.) spin-orbital coupling (SOC) and with SOC. (b) 3D band structure of Ni_3InN. (c) Temperature-dependent resistivity (ρ) of Ni_3InN thin films on various substrates. The temperature-dependent ρ of $La_{2-x}Sr_xCuO_4$, $SrRuO_3$, and Sr_2RuO_4 are included as benchmarks for typical correlated metallic behavior in perovskite oxides to highlight the exceptional electronic stability of Ni_3InN. (d) Optical conductivities of Ni_3InN thin films on various substrates, obtained from spectroscopic ellipsometry at room-temperature. The arrows indicate the optical excitation peaks. (e) Schematic of band structure, extracted from optical conductivity measurements.

the high crystalline quality and sharp interfaces, but also reveals microscopic interfacial configurations such as strain-induced lattice distortions and atomically defined bonding at the heterointerfaces. This fundamental distinction highlights that, whereas oxides are suited for smooth strain engineering, Ni_3InN-based films offer a pathway for strain-mediated control of crystalline orientation, thereby opening opportunities for designing antiperovskite heterostructures with tunable anisotropic properties. Electrically, the Ni_3InN thin films exhibit exceptional conductivity and maintain a remarkably stable resistivity across an extensive temperature spectrum. This characteristic renders them highly appropriate for applications including high-accuracy resistors, stable sensors, and other high-precision instruments that function within various temperature conditions. Together, these findings establish Ni_3InN thin films as a new experimental platform for probing emergent electronic phenomena at the intersection of perovskite physics and antiperovskite chemistry. By uniting epitaxial stabilization, interface-sensitive growth, and detailed theoretical modeling, our work opens a pathway to discover novel correlated phases in anti-perovskite nitrides and demonstrates their potential as a counterpart to oxide perovskites in the quest for exotic quantum states, paving the way for their integration into next-generation electronic and spintronic devices.

4 | Methods

4.1 | Synthesis of High-Quality Epitaxial Nitride Thin Films

Polycrystalline Ni_3InN targets were synthesized through a high-pressure reaction route using a mixture of In_2O_3, Ni and $NaNH_2$ powders. The mixed powder was sintered at 5 GPa and 900°C for 60 min at the High-Pressure Lab of South University of Science and Technology (SUSTech). Powder X-ray diffraction measurements on the target demonstrate a stoichiometric and correct chemical composition. Single-crystalline antiperovskite nitride Ni_3InN thin films were fabricated by pulsed laser deposition (PLD) using a XeCl excimer laser with a 308 nm wavelength. During the thin-film deposition, the energy density and laser frequency are maintained at ~1.6 J/cm^2 and 5 Hz. To systematically

investigate the effects of strain on Ni_3InN thin films, all films were grown on (001)-oriented $LaAlO_3$, $SrTiO_3$, and (011)-oriented $DyScO_3$ substrates at a temperature of 500°C and a base pressure of 1×10^{-8} Torr. The thickness of the Ni_3InN film, approximately 30 nm, was controlled by counting the number of laser pulses and further confirmed by X-ray reflectometry. The samples were cooled down slowly to room-temperature at a rate of–5°C under high-vacuum atmosphere ($\sim 10^{-7}$-10^{-8} Torr), keeping the same as the growth conditions.

4.2 | Structural Characterization and Electronic State Measurements

The thin-film quality was examined by a high-resolution four-circle X-ray diffractometer (Malvern Panalytical, X'Pert3 MRD) with θ –2θ line scans and rocking curve scans. Phi scans and off-specular RSM are conducted to determine the epitaxial growth and in-plane strain states of Ni_3InN thin films. The temperature-dependent X-ray diffraction (XRD) was measured using a Bruker D8 Discovery diffractometer. X-ray reflectivity (XRR) measurements were performed to check the layer thickness and interface roughness. Electrical measurements, including temperature-dependent resistivity, magnetoresistance (MR), and Hall resistance, were conducted in a Physical Property Measurement System (PPMS), using the standard van der Pauw method. The optical conductivity of different strained RP nickelate thin films was measured at room-temperature using a commercial optical ellipsometer (J. A. Woollam Co., Inc.).

4.3 | STEM Characterizations and Analysis

Cross-sectional transmission electron microscopy (TEM) samples were fabricated by standard ion beam (FIB) lift-off process and measured in scanning mode using a JEM ARM 200CF microscope at the Institute of Physics, Chinese Academy of Sciences. The high-angle annular dark field (HAADF) images were collected along [100] and [110] orientation for confirming the crystal structure. All scanning transmission electron microscopy (STEM) images were analyzed using Gatan DigitalMicrograph. Electron-energy-loss-spectroscopy (EELS) mappings were performed at Ni *L*-, In *L*-, La *M*-, Al *K*-, Sr *L*-and Ti *L*-edges to evaluate the interfacial mixing.

4.4 | First-Principles Calculations

Density-Functional Theory (DFT) [52, 57] calculations were performed to investigate the structural relaxation, electronic structure, and elastic properties of X_3InN materials. The simulations were conducted using the Vienna Ab initio Simulation Package (VASP) [53, 54] and WIEN2k [55, 56], employing the Perdew–Burke–Ernzerhof (PBE) form of the Generalized Gradient Approximation (GGA) for the exchange-correlation functional [58]. A plane-wave energy cutoff of 500 eV and a Monkhorst-Pack *k*-point mesh of 13 × 13 × 13 were used for Brillouin zone integration. Phonon spectra were computed using both the frozen-phonon (finite displacement) method [59] and density-functional perturbation theory (DFPT) [60], implemented via the Phonopy package [61] interfaced with VASP, based on the relaxed ground-state structures of each X_3InN compound.

Acknowledgements

We thank Ling Lu's group at IOP-CAS for helping the optical conductivity measurements and Shuai Dong's group at Southeast University for general theoretical inputs. This work was supported by the Beijing Natural Science Foundation (Grant Nos. JQ24002 to E.J.G. and IS25040 to S.Choi), the National Natural Science Foundation of China (Grant Nos. 12422407 to L.S., U22A20263 and 52250308 to E.J.G., 12304158 to Q.J., and 12474096 to C.W.), the National Key Basic Research Program of China (Grant No. 2020YFA0309100 to E.J.G.), the CAS Project for Young Scientists in Basic Research (Grant No. YSBR-084 to E.J.G.), the Guangdong Basic and Applied Basic Research Foundation (Grant No. 2022B1515120014 to E.J.G.), the Guangdong-Hong Kong-Macao Joint Laboratory for Neutron Scattering Science and Technology, the China Postdoctoral Science Foundation (Grant No. 2022M723353 to E.J.G.), and the International Young Scientist Fellowship of IOP-CAS to S.Choi. Theoretical calculations have been mainly done in Northwest University (Xi'an).

Conflicts of Interest

The authors declare no conflicts of interest.

Data Availability Statement

All data needed to evaluate the conclusions in the paper are present in the paper and/or the Supplementary Materials. Additional datasets generated during and/or analyses during the current study are available from the first author (T.C.) and corresponding authors (L.S., E.J.G., and K.J.J.) on reasonable request. Supplementary information is available in the online version of the paper. Reprint and permission information is available online. Certain commercial equipments are identified in this paper to foster understanding.

References

1. T. Ito, H. Takagi, S. Ishibashi, T. Ido, and S. Uchida, "Normal-State Conductivity Between CuO_2 Planes In Copper Oxide Superconductors," *Nature* 350 (1991): 596–598, https://doi.org/10.1038/350596a0.

2. A. P. Mackenzie, R. K. W. Haselwimmer, A. W. Tyler, et al., "Extremely Strong Dependence Of Superconductivity On Disorder In Sr_2RuO_4," *Physical Review Letters* 80 (1998): 161–164, https://doi.org/10.1103/PhysRevLett.80.161.

3. K. I. Kobayashi, T. Kimura, H. Sawada, K. Terakura, and Y. Tokura, "Room-Temperature Magnetoresistance in an Oxide Material with an Ordered Double-Perovskite Structure," *Nature* 395 (1998): 677–680, https://doi.org/10.1038/27167.

4. P. Schiffer, A. P. Ramirez, W. Bao, and S. W. Cheong, "Low-Temperature Magnetoresistance And The Magnetic Phase Diagram Of La_1_xCaxMnO_3," *Physical Review Letters* 75 (1995): 3336–3339, https://doi.org/10.1103/PhysRevLett.75.3336.

5. M. Imada, A. Fujimori, and Y. Tokura, "Metal-Insulator Transitions," *Reviews of Modern Physics* 70 (1998): 1039–1263, https://doi.org/10.1103/RevModPhys.70.1039.

6. A. P. Mackenzie, S. R. Julian, A. J. Diver, et al., "Quantum Oscillations In The Layered Perovskite Superconductor Sr_2RuO_4," *Physical Review Letters* 76 (1996): 3786–3789, https://doi.org/10.1103/PhysRevLett.76.3786.

7. J. A. Bert, B. Kalisky, C. Bell, et al., "Direct Imaging of the Coexistence of Ferromagnetism and Superconductivity at the $LaAlO_3/SrTiO_3$ Interface," *Nature Physics* 7 (2011): 767–771, https://doi.org/10.1038/nphys2079.

8. A. Ohtomo and H. Y. Hwang, "A High-Mobility Electron Gas at the $LaAlO_3/SrTiO_3$ Heterointerface," *Nature* 427 (2004): 423–426, https://doi.org/10.1038/nature02308.

9. M. Gibert, P. Zubko, R. Scherwitzl, J. Íñiguez, and J. M. Triscone, "Exchange Bias In $LaNiO_3$–$LaMnO_3$ Superlattices," *Nature Materials* 11 (2012): 195–198, https://doi.org/10.1038/nmat3224.

10. R. Xu, S. Liu, I. Grinberg, et al., "Ferroelectric Polarization Reversal via Successive Ferroelastic Transitions," *Nature Materials* 14 (2015): 79–86, https://doi.org/10.1038/nmat4119.

11. D. Li, K. Lee, B. Y. Wang, et al., "Superconductivity in an Infinite-Layer Nickelate," *Nature* 572 (2019): 624–627, https://doi.org/10.1038/s41586-019-1496-5.

12. H. Sun, M. Huo, X. Hu, et al., "Signatures of Superconductivity NEAR 80 K in a Nickelate Under High Pressure," *Nature* 621 (2023): 493–498, https://doi.org/10.1038/s41586-023-06408-7.

13. Y. Zhu, D. Peng, E. Zhang, et al., "Superconductivity In Pressurized Trilayer $La_4Ni_3O_{10-\delta}$ Single Crystals," *Nature* 631 (2024): 531–536, https://doi.org/10.1038/s41586-024-07553-3.

14. T. Cui, S. Choi, T. Lin, et al., "Strain-Mediated Phase Crossover in Ruddlesden–Popper Nickelates," *Communications Materials* 5 (2024): 32, https://doi.org/10.1038/s43246-024-00478-4.

15. M. Jiang, M. Berciu, and G. A. Sawatzky, "Stabilization of Singlet Hole-Doped State in Infinite-Layer Nickelate Superconductors," *Physical Review B* 106 (2022): 115150, https://doi.org/10.1103/PhysRevB.106.115150.

16. M. Jiang, M. Berciu, and G. A. Sawatzky, "Critical Nature Of The Ni Spin State In Doped $NdNiO_2$," *Physical Review Letters* 124 (2020): 207004, https://doi.org/10.1103/PhysRevLett.124.207004.

17. H. Nakamura, D. Huang, and H. Takagi, "Molecular Beam Epitaxy of Antiperovskite Oxides," *APL Materials* 10 (2022): 060904, https://doi.org/10.1063/5.0096680.

18. W. Wu, N. G. Combs, and S. Stemmer, "Revealing the Intrinsic Transport Properties of Antiperovskite Sr_3SnO Thin Films," *Applied Physics Letters* 121 (2022): 233101, https://doi.org/10.1063/5.0128316.

19. T. H. Hsieh, J. Liu, and L. Fu, "Topological Crystalline Insulators and Dirac Octets in Antiperovskites," *Physical Review B* 90 (2014): 081112, https://doi.org/10.1103/PhysRevB.90.081112.

20. M. Oudah, A. Ikeda, J. N. Hausmann, et al., "Superconductivity In The Antiperovskite Dirac-Metal Oxide $Sr_{3-x}SnO$," *Nature Communications* 7 (2016): 13617, https://doi.org/10.1038/ncomms13617.

21. Y. Wen, M. Chen, D. Gu, et al., "First-Principles Study Of The Structural, Electronic, And Magnetic Properties Of Mn-Doped Ni_3XN (X = Al, Cu, In) Compounds," *Solid State Communications* 325 (2021): 114168, https://doi.org/10.1016/j.ssc.2020.114168.

22. C. X. Quintela, K. Song, D. F. Shao, et al., "Epitaxial Antiperovskite/Perovskite Heterostructures for Materials Design," *Science Advances* 6 (2020): aba4017.

23. K. Takenaka, T. Inagaki, and H. Takagi, "Conversion of Magnetic Structure by slight Dopants in Geometrically Frustrated Antiperovskite Mn_3GaN," *Applied Physics Letters* 95 (2009): 132508, https://doi.org/10.1063/1.3243340.

24. D. Boldrin, E. Mendive-Tapia, J. Zemen, et al., "Multisite Exchange-Enhanced Barocaloric Response In Mn_3NiN," *Physical Review X* 8 (2018): 041035.

25. C. X. Quintela, N. Campbell, D. F. Shao, et al., "Epitaxial Thin Films of Dirac Semimetal Antiperovskite Cu_3PdN," *APL Materials* 5 (2017): 096103.

26. K. Takenaka and H. Takagi, "Giant Negative Thermal Expansion in Ge-Doped Anti-Perovskite Manganese Nitrides," *Applied Physics Letters* 87 (2005): 261902, https://doi.org/10.1063/1.2147726.

27. A. Ji, C. Li, and Z. Cao, "Ternary Cu_3NPd_x Exhibiting Invariant Electrical Resistivity Over 200 K," *Applied Physics Letters* 89 (2006): 252120, https://doi.org/10.1063/1.2422882.

28. T. Nan, C. X. Quintela, J. Irwin, et al., "Controlling Spin Current Polarization Through Non-Collinear Antiferromagnetism," *Nature Communications* 11 (2020): 4671, https://doi.org/10.1038/s41467-020-17999-4.

29. M. Y. Chern, D. A. Vennos, and F. J. Disalvo, "Synthesis, Structure, and Properties of Anti-Perovskite Nitrides Ca_3MN, M = P, As, Sb, Bi, Ge, Sn, And Pb," *Journal of Solid State Chemistry* 96 (1992): 415–425, https://doi.org/10.1016/S0022-4596(05)80276-2.

30. T. Hajiri, K. Matsuura, K. Sonoda, E. Tanaka, K. Ueda, and H. Asano, "Spin-Orbit-Torque Switching of Noncollinear Antiferromagnetic Antiperovskite Manganese Nitride Mn3GaN," *Physical Review Applied* 16 (2021): 024003, https://doi.org/10.1103/PhysRevApplied.16.024003.

31. H. Lee, H. Sukegawa, J. Liu, et al., "Ferromagnetic MnGaN Thin Films with Perpendicular Magnetic Anisotropy for Spintronics Applications," *Applied Physics Letters* 107 (2015): 032403, https://doi.org/10.1063/1.4927097.

32. T. Hajiri, S. Ishino, K. Matsuura, and H. Asano, "Electrical Current Switching Of The Noncollinear Antiferromagnet Mn_3GaN," *Applied Physics Letters* 115 (2019): 052403, https://doi.org/10.1063/1.5109317.

33. Z. F. Hou, "Elastic properties and electronic structures of antiperovskite-type InNCo3 and InNNi3," *Solid State Communications* 150 (2010): 1874–1879, https://doi.org/10.1016/j.ssc.2010.07.047.

34. N. Pandech, K. Sarasamak, and S. Limpijumnong, "Elastic Properties Of Perovskite $ATiO_3$ (A = Be, Mg, Ca, Sr, And Ba) And $PbBO_3$ (B = Ti, Zr, And Hf): First-Principles Calculations," *Journal of Applied Physics* 117 (2015): 174108, https://doi.org/10.1063/1.4919837.

35. L. Stixrude, C. Lithgow-Bertelloni, B. Kiefer, and P. Fumagalli, "Phase Stability And Shear Softening In $CaSiO_3$ Perovskite At High Pressure," *Physical Review B* 75 (2007): 024108, https://doi.org/10.1103/PhysRevB.75.024108.

36. T. Maekawa, K. Kurosaki, and S. Yamanaka, "Physical Properties Of Polycrystalline $SrVO_{3-\delta}$," *Journal of Alloys and Compounds* 426 (2006): 46–50, https://doi.org/10.1016/j.jallcom.2006.02.026.

37. N. Orlovskaya, M. Lugovy, S. Pathak, et al., "Thermal And Mechanical Properties Of $LaCoO_3$ And $La_{0.8}Ca_{0.2}CoO_3$ Perovskites," *Journal of Power Sources* 182 (2008): 230–239, https://doi.org/10.1016/j.jpowsour.2008.03.072.

38. P. Kulandaivelu, K. Sakthipandi, P. S. Kumar, and V. Rajendran, "Mechanical Properties Of Bulk And Nanostructured $La_{0.61}Sr_{0.39}MnO_3$ Perovskite Manganite Materials," *Journal of Physics and Chemistry of Solids* 74 (2013): 205–214, https://doi.org/10.1016/j.jpcs.2012.09.008.

39. V. Rajendran, S. Muthu Kumaran, V. Sivasubramanian, T. Jayakumar, and B. Raj, "Anomalies In Elastic Moduli And Ultrasonic Attenuation Near Ferromagnetic Transition Temperature In $La_{0.67}Sr_{0.33}MnO_3$ Perovskite" *physica status solidi (a)* 195 (2003): 350–358, https://doi.org/10.1002/pssa.200305931.

40. P. Su, H. Wen, Y. Zhang, et al., "Super-Flexibility In Freestanding Single-Crystal $SrRuO_3$ Conductive Oxide Membranes," *ACS Applied Electronic Materials* 4 (2022): 2987–2992, https://doi.org/10.1021/acsaelm.2c00422.

41. R. Zhang, L. Bai, X. Xie, et al., "Prediction Of The Hardest $BiFeO_3$ From First-Principles Calculations," *Physical Chemistry Chemical Physics* 25 (2023): 5049–5055, https://doi.org/10.1039/D2CP05817K.

42. X. Hu, S. Yan, X. Lu, F. Huang, and S. Xiao, "Enhanced Mechanical Hardness Of Mixed-Phase $BiFeO_3$ Films Through Quenching," *Acta Materialia* 283 (2025): 120539, https://doi.org/10.1016/j.actamat.2024.120539.

43. H. Yamaguchi, J. Tatami, and M. Iijima, "Measurement Of Mechanical Properties Of $BaTiO_3$ Layer In Multi-Layered Ceramic Capacitor Using A Microcantilever Beam Specimen," *Journal of the Ceramic Society of Japan* 127 (2019): 335–338, https://doi.org/10.2109/jcersj2.19030.

44. M. Fukuhara and Y. Abe, "High-Temperature Elastic Moduli and Internal Frictions of ?-SiC Ceramic," *Journal of Materials Science Letters* 12 (1993): 681–683, https://doi.org/10.1007/BF00465591.

45. M. Fukuhara and A. Sanpei, "Elastic Moduli and Internal Frictions of Inconel 718 and Ti-6Al-4 V as a Function of Temperature," *Journal of Materials Science Letters* 12 (1993): 1122–1124, https://doi.org/10.1007/BF00420541.

46. G. N. Greaves, A. L. Greer, R. S. Lakes, and T. Rouxel, "Poisson's Ratio and Modern Materials," *Nature Materials* 10 (2011): 823–837, https://doi.org/10.1038/nmat3134.

47. E. Ferretti, "Active Confinement of Masonry Walls With Stainless Steel Straps: The Effect of Strap Arrangement on the in-Plane Behavior of Strength, Poisson's Ratio, and Pseudo-Ductility," *Buildings* 13 (2023): 3027, https://doi.org/10.3390/buildings13123027.

48. T. Gorges, T. Weber, J. Mayer, and P. Motzki, "Experimental Investigation of Phase-Dependent Resistivity and Poisson's Ratio in Shape Memory Alloy Wires," *Smart Materials and Structures* 34 (2025): 065033, https://doi.org/10.1088/1361-665X/ade580.

49. Y. L. Hao, S. J. Li, B. B. Sun, M. L. Sui, and R. Yang, "Ductile Titanium Alloy with Low Poisson's Ratio," *Physical Review Letters* 98 (2007): 216405, https://doi.org/10.1103/PhysRevLett.98.216405.

50. J. Y. Chauleau, E. Haltz, C. Carretero, S. Fusil, and M. Viret, "Multi-Stimuli Manipulation of Antiferromagnetic Domains Assessed by Second-Harmonic Imaging," *Nature Materials* 16 (2017): 803–807, https://doi.org/10.1038/nmat4899.

51. H. N. Lee, H. M. Christen, M. F. Chisholm, C. M. Rouleau, and D. H. Lowndes, "Strong Polarization Enhancement in Asymmetric Three-Component Ferroelectric Superlattices," *Nature* 433 (2005): 395–399, https://doi.org/10.1038/nature03261.

52. W. Kohn and L. J. Sham, "Self-Consistent Equations Including Exchange and Correlation Effects," *Physical Review* 140 (1965): A1133–A1138, https://doi.org/10.1103/PhysRev.140.A1133.

53. G. Kresse and J. Furthmüller, "Efficiency of ab-initio Total Energy Calculations for Metals and Semiconductors Using a Plane-Wave Basis Set," *Computational Materials Science* 6 (1996): 15–50, https://doi.org/10.1016/0927-0256(96)00008-0.

54. G. Kresse and J. Furthmüller, "Efficient Iterative Schemes for ab initio Total-Energy Calculations Using a Plane-Wave Basis Set," *Physical Review B* 54 (1996): 11169–11186, https://doi.org/10.1103/PhysRevB.54.11169.

55. P. Blaha, K. Schwarz, and G. K. H. Madsen, *WIEN2k, An Augmented Plane Wave + Local Orbitals Program for Calculating Crystal Properties* (Karlheinz Schwarz, Techn. Universität Wien, 2001).

56. K. Schwarz, "DFT Calculations of Solids With LAPW and WIEN2k," *Journal of Solid State Chemistry* 176 (2003): 319–328, https://doi.org/10.1016/S0022-4596(03)00213-5.

57. P. Hohenberg and W. Kohn, "Inhomogeneous Electron Gas," *Physical Review* 136 (1964): B864.

58. J. P. Perdew, K. Burke, and M. Ernzerhof, "Generalized Gradient Approximation Made Simple," *Physical Review Letter* 77 (1996): 3865.

59. L. Chaput, A. Togo, and I. Tanaka, "Finite-Displacement Computation of the Electron-Phonon Interaction within the Projector Augmented-Wave Method," *Physical Review B* 100 (2019): 174304, https://doi.org/10.1103/PhysRevB.100.174304.

60. S. Baroni, S. de Gironcoli, A. Dal Corso, and P. Giannozzi, "Phonons and Related Crystal Properties from Density-Functional Perturbation Theory," *Reviews of Modern Physics* 73 (2001): 515–562, https://doi.org/10.1103/RevModPhys.73.515.

61. A. Togo and I. Tanaka, "First Principles Phonon Calculations in Materials Science," *Scripta Materialia* 108 (2015): 1–5, https://doi.org/10.1016/j.scriptamat.2015.07.021.

Supporting Information

Additional supporting information can be found online in the Supporting Information section.

Supporting File: adfm75034-sup-0001-SuppMat.docx.